ISBN: 978-628-96613-3-0. ISSN: 2414-6390. Digital Object Identifier: https://dx.doi.org/10.18687/LACCEI2026.1.1.2767

Hybrid RBF Neural Network and Multi-Level Genetic Algorithm for MPPT Optimization in Photovoltaic Systems with IHGM-SEPIC Converter: Experimental Validation

Luis Ernesto Neira-Ropero[1], Aldo Pardo García1[2] and Jorge Luis Diaz Rodriguez[3]
[1, 2, 3] *Universidad de Pamplona, facultad de Ingenierías y Arquitectura, Pamplona, Norte de Santander, Colombia*
luis.neira@unipampona.edu.co, apardo13@unipamplona.edu.co, jdiazcu@unipamplona.edu.co

Abstract*– This paper presents a hybrid Maximum Power Point Tracking (MPPT) system that combines Radial Basis Function (RBF) neural networks with a multi-level Genetic Algorithm (GA) for photovoltaic (PV) system optimization. The proposed approach is implemented on embedded hardware (ESP32-S3 and Raspberry Pi 5) coupled with an Interleaved High-Gain Modified SEPIC (IHGM-SEPIC) converter, achieving a measured efficiency of 98.87%. A complete mathematical model of the IHGM-SEPIC topology is derived, comprising 16 state equations. The GA simultaneously optimizes converter parameters, MPPT control parameters, and RBF network weights using BLX-α crossover, adaptive mutation, and tournament selection with a multi-objective fitness function. Experimental validation was conducted using a 100W monocrystalline panel under real Andean highland conditions (Pamplona, Colombia, 2340 (m.a.s.l.) over a dataset of 5,629 records. Results demonstrate 4.67% improvement over conventional P&O and 7.37% over commercial controllers in tracking efficiency, with a response time of 0.8 seconds versus 3.5 seconds for P&O. Statistical validation from N=30 GA executions confirms convergence reliability with σ = 0.35%.

Keywords-- MPPT, RBF Neural Network, Genetic Algorithm, IHGM-SEPIC, Embedded Systems.

I. INTRODUCTION

Photovoltaic (PV) energy systems have experienced exponential growth globally, yet their efficiency remains critically dependent on Maximum Power Point Tracking (MPPT) algorithms. Traditional approaches such as Perturb and Observe (P&O) and Incremental Conductance (IC) suffer from oscillation around the MPP, slow response to rapid irradiance changes, and failure under partial shading conditions [1], [2], [3]. These limitations are particularly pronounced in Andean highland environments where altitude (>2,000 m.a.s.l.), rapid cloud transients, and temperature variations create uniquely challenging operating conditions [4], [5].

Recent advances in artificial intelligence-based MPPT have demonstrated promising results. Hybrid approaches combining neural networks with metaheuristic optimization have emerged as a dominant trend in Q1 publications. Notable examples include RBF networks with Particle Swarm Optimization (RBF-PSO) [6], [7], Deep Learning MPPT controllers [8], and hybrid Model Predictive Control (MPC) approaches [9]. However, the simultaneous optimization of converter topology, control parameters, and neural network architecture remains an open challenge. Additionally, the development of IoT-based prototyping environments has enabled rapid validation of embedded energy systems, as discussed in [10].

This paper proposes a novel hybrid MPPT system that addresses this gap through three key contributions (Fig. 1): (1) a multi-level Genetic Algorithm that simultaneously optimizes the IHGM-SEPIC converter parameters, MPPT control gains, and RBF network weights; (2) a complete equation mathematical model for the IHGM-SEPIC converter topology; and (3) experimental validation on embedded hardware under real Andean highland conditions in Pamplona, Colombia (7°18'N, 72°39'W, 2,340 m.a.s.l.).

II. SYSTEM ARCHITECTURE

A. PV Panel and Operating Conditions

The experimental platform utilizes a 100W monocrystalline PV panel with V_{mpp} = 18.5V and I_{mpp} = 5.41A. Data acquisition comprises 5,629 records collected in November 2025 under Andean highland conditions characterized by irradiance levels ranging from 200 to 1,050 W/m² and ambient temperatures between 8°C and 24°C [11].

B. IHGM-SEPIC Converter Topology

The Interleaved High-Gain Modified SEPIC (IHGM-SEPIC) converter was selected for its positive output polarity, high voltage gains, and reduced input current ripple. The target output is 48V from the panel's 18.5V nominal MPP voltage, requiring a voltage gain of M = 2.595. The nominal duty cycle is calculated as D = 0.443 at a switching frequency of $f_{sw} = 50\ kHz$.

The voltage gain of the IHGM-SEPIC converter is given by:

$$M(D) = V_{out}/V_{in} = {(1 + D)}\big/{(1 - D)} \tag{1}$$

The complete state-space representation involves equations describing the inductor currents (i_{L1}, i_{L2}, i_{L3}), capacitor voltages $(V_{C1}, V_{C2}, V_{C3}, V_{out})$, and their interactions during switching and non-switching intervals. The state vector is defined as:

$$x = [i_{L1}, i_{L2}, i_{L3}, v_{L2}, v_{L3}, v_{L1}, v_{out}]^T \tag{2}$$

Fig. 2 presents the key voltage and current waveforms of the IHGM-SEPIC converter over two switching periods. The gate signal V_{vs} defines the ON interval $(0 < t < DT_s)$ and OFF interval $(DT_s < t < T_s)$. During the ON interval, inductor currents i_{L1}, i_{L2} increase linearly while i_{L3} operates with 180° phase shift due to interleaving, achieving partial ripple cancellation at the input. The intermediate capacitor voltage v_{C1} and output voltage V_{out} show complementary charging/discharging behavior. These waveforms inform the state equations that follow [12].

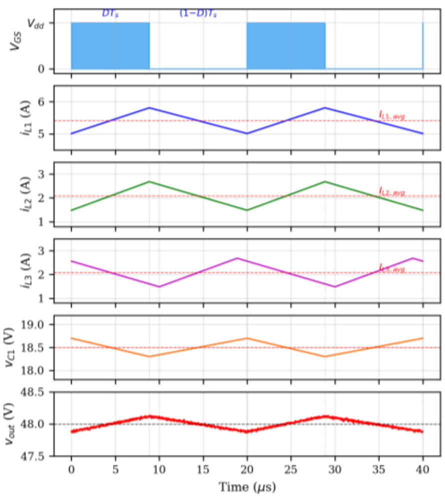

Fig. 1. Key voltage and current waveforms of the IHGM-SEPIC converter (D=0.443, f_sw=50 kHz).

During the ON interval ($0 < t < DT_s$), the inductor L_1 charges from the input, and the coupled inductors L_2 and L_3 transfer energy to the intermediate capacitors. The state equations for this interval are:

$$L_1 * \frac{di_{L1}}{dt} = V_{PV} - r_{L1} * i_{L1} \tag{3}$$

$$L_2 * \frac{di_{L2}}{dt} = V_{C1} - r_{L2} * i_{L2} \tag{4}$$

$$C_{out} * \frac{dv_{out}}{dt} = i_{L2} + i_{L3} - \frac{v_{out}}{R} \tag{5}$$

The critical inductance and capacitance values to ensure Continuous Conduction Mode (CCM) are:

$$L_{1,crit} = {R(1-D)^2}\Big/{(2f_{sw}(1+D)^2)} \tag{6}$$

$$C_{out\_min} = {D}/{R * \Delta v_{out} - f_{sw}} \tag{7}$$

During the OFF interval ($DT_s < t < T_s$), the switch opens and the stored energy in the inductors is transferred to the output through the diodes. The state equations become:

$$L_1 * {di_{L1}}/{dt} = V_{PV} - v_{C1} - v_{out} - r_{L1} * i_{L1} \tag{8}$$

$$L_2 * {di_{L2}}/{dt} = -v_{C2} - v_{out} - r_{L2} * i_{L2} \tag{9}$$

$$C_1 * {dv_{C1}}/{dt} = i_{L1} - i_{L3} \tag{10}$$

Applying the state-space averaging technique over one switching period, the averaged model is expressed in matrix form as:

$$\frac{d\bar{x}}{dt} = \left[D * A_{on} + (1-D) * A_{off}\right] * \bar{x} + \left[D * B_{on} + (1-D) * B_{off}\right] * u \tag{11}$$

where A_{on}, A_{off} are the 7×7 state matrices for ON and OFF intervals respectively, and B_{on}, B_{off} are the corresponding input matrices. The small-signal transfer function $G_{vd}(s)$ is obtained by linearization around the operating point:

$$G_{vd}(s) = C * (sI - A)^{-1} * [(A_{on} - A_{off}) * X + (B_{on} - B_{off}) * U] \tag{12}$$

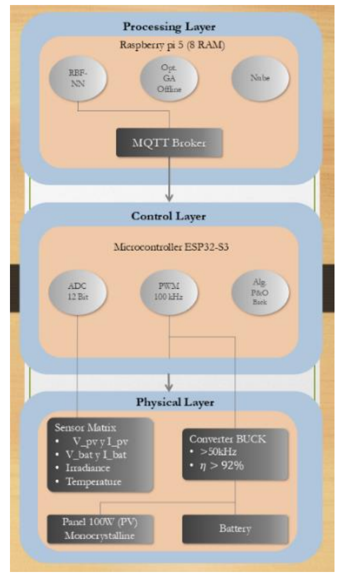

Fig. 2. General system scheme

Table I presents the optimized component values obtained from the GA Level 1 optimization. The table includes the search space bounds $[X_{min}, X_{max}]$ imposed on each variable during the GA optimization, the resulting GA-optimized values, the analytically calculated minimums for CCM operation, and the design margin. The bounds were established based on commercial component availability and the analytical constraints from (6) and (7).

TABLE I
GA-*OPTIMIZED IHGM-SEPIC COMPONENT VALUES WITH SEARCH BOUNDS*

Param.	Symbol	x_min	x_max	GA Val.	Calc.	Unit	Margin
Inductor 1	L_1	100	500	330	285	μH	15.8%
Inductor 2	L_2	100	400	220	190	μH	15.8%
Inductor 3	L_3	100	400	220	190	μH	15.8%
Capacitor 1	C_1	22	220	100	82	μF	22.0%
Capacitor 2	C_2	22	220	100	82	μF	22.0%
Capacitor 3	C_3	10	100	47	38	μF	23.7%
Output Cap.	C_o^5 □	220	1000	470	412	μF	14.1%

Fig. 3. DC/DC converter test module

C. RBF Neural Network Architecture

The RBF network employs a 7-20-1 architecture where 7 inputs capture PV voltage, current, power, irradiance, temperature, and time-derivative features ($\Delta V/\Delta t$, $\Delta I/\Delta t$). The hidden layer consists of 20 Gaussian neurons with adaptive centers μ_j and widths σ_j. The output layer produces the optimal duty cycle D_{opt}. The RBF activation function is:

$$\varphi j(x) = \exp(-\|x - \mu j\|^2 / (2\sigma j^2)) \tag{13}$$

$$D_{opt} = \sum_{j=1^{20}} wj * \varphi j(x) + b \tag{14}$$

III. MULTI-LEVEL GENETIC ALGORITHM OPTIMIZATION

The proposed multi-level GA simultaneously optimizes three parameter groups: (Level 1) IHGM-SEPIC converter component values (L_1, L_2, L_3, C_1, C_2, C_3, C_{out}); (Level 2) MPPT control parameters (step size, perturbation frequency); and (Level 3) RBF network parameters (centers μ_j, widths σ_j, weights w_j, bias b).

A. Chromosome Encoding and Operators

Each chromosome encodes 7 converter parameters + 2 MPPT parameters + 61 RBF parameters (20 centers × 1 + 20 widths + 20 weights + 1 bias) = 70 real-valued genes. The GA employs the following operators:

BLX-α Crossover: For parents p_1 and p_2, offspring gene c_i is sampled uniformly from $[\min(p_{1i},p_{2i}) - \alpha\cdot d, \max(p_{1i},p_{2i}) + \alpha\cdot d]$, where $d = |p_{1i} - p_{2i}|$ and $\alpha = 0.5$.

Adaptive Mutation: The mutation rate ρ(g) decreases over generations:

$$\rho(g) = \rho max - (\rho max - \rho min) * (g/G) \tag{15}$$

Where $\rho_{max} = 0.15$, $\rho_{min} = 0.01$, g is the current generation, and G = 100 is the total generations. Tournament selection with size k = 3 is applied.

B. Multi-Objective Fitness Function

The design of the fitness function is critical to the GA's ability to balance competing objectives. In MPPT systems, maximizing power extraction must be simultaneously achieved with minimal converter stress, stable output voltage, and fast transient response. We formulate a weighted-sum multi-objective function where each term is normalized to [0, 1]:

$$F = w_1 * \eta_{MPPT} + w_2 * \eta_{CONV} - w_3 \cdot \Delta V_{rms} - w_4 * t_r \tag{16}$$

Each component of (16) is defined as follows. The MPPT tracking efficiency η_{MPPT} measures the ratio of extracted power to the theoretical maximum:

$$\eta_{MPPT} = (1/N) * \sum_{k=1^N} {P_{actual}(k)}\Big/{P_{MPP}(k)} \tag{17}$$

The converter efficiency η_{conv} accounts for conduction losses in inductors (r_L), MOSFET on-resistance ($R_{DS(on)}$), and diode forward voltage drops:

$$\eta_{conv} = \frac{P_{out}}{(P_{out} + P_{cond} + P_{sw} + P_{diode})} \tag{18}$$

The RMS voltage regulation error ΔV_{rms} is normalized by the reference voltage V_{ref} = 48V:

$$\Delta V_{rms} = \sqrt{{\left[(1/N) * \sum\left(v_{out}(k) - V_{ref}\right)^2\right]}\Big/{V_{ref}}} \tag{19}$$

The normalized rise time $\hat{t}_r$ penalizes slow tracking response, with T_{max} = 5s as the maximum acceptable response time:

$$\hat{t}_r = {t_r}/{T_{max}} \tag{20}$$

The weights $w_1 = 0.4$, $w_2 = 0.3$, $w_3 = 0.2$, $w_4 = 0.1$ were determined empirically through sensitivity analysis, prioritizing tracking efficiency (40%) and converter efficiency (30%) while penalizing voltage deviation (20%) and slow response (10%). This weighting ensures that $F \in [0, 1]$, with F = 1 representing the theoretical optimum.

IV. EMBEDDED IMPLEMENTATION

The system (Fig. 3) is deployed on a dual-processor embedded platform. The ESP32-S3 microcontroller handles real-time sensor acquisition using 4-20mA industrial transducers (voltage: JXDA4U, current: JXK-10) with 32-bit ADC resolution via an ADS1263 module, and PWM generation at 50 kHz. The Raspberry Pi 5 executes RBF neural network inference in Python (forward propagation < 2 ms), GA optimization, and data logging via InfluxDB 2.0 and Node-RED dashboards [13]. Communication employs MQTT protocol over WiFi at 100 Hz [14].

The GA runs offline during calibration (~45 seconds for 50 individuals, 100 generations, parallelized across 4 CPU cores). It is acknowledged that using both an ESP32-S3 and Raspberry Pi 5 represents a higher resource investment compared to single-microcontroller solutions (Table II). However, this architecture enables separation of concerns: the ESP32-S3 handles deterministic real-time tasks (ADC, PWM) while the Raspberry Pi 5 provides computational capacity for RBF inference, GA optimization, and SCADA visualization—functions infeasible on a single microcontroller. The 7.37% efficiency gain over commercial controllers translates to ~73.7 Wh/day additional energy harvest for a 100W panel, yielding ROI within 6–12 months.

The experimental dataset comprises 5,629 records from November 2025, sampled at 1-second intervals during daylight hours (6:00-18:00), including PV voltage, current, power, irradiance, temperatures, humidity, duty cycle, and output measurements. Preprocessing involved 3σ outlier removal, [0,1] normalization, and 70/15/15 training/validation/test split.

V. RESULTS AND ANALYSIS

A. GA Convergence Analysis

Fig. 4 shows the overall GA convergence over 100 generations from N=30 independent runs. The algorithm achieves 95% of its final fitness value by generation 40, with full convergence by generation 70. The narrow confidence band ($\sigma < 0.005$ after generation 60) confirms the robustness of the optimization process.

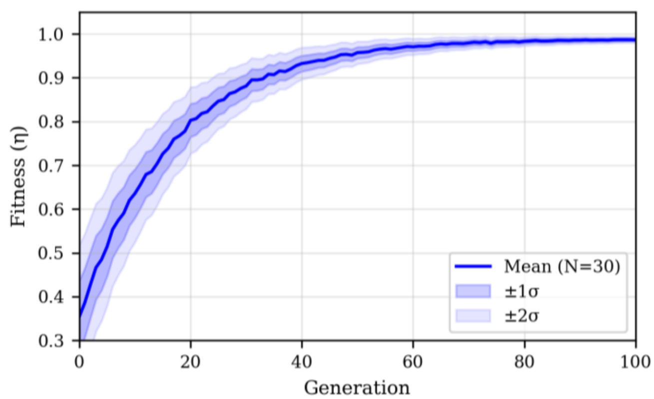

Fig. 4. Multi-level GA convergence over 100 generations (N=30 runs).

To provide deeper insight into the GA dynamics, Fig. 5 decomposes the convergence by hierarchical level. Level 1 (converter parameters, $n_p = 7$) converges fastest due to the smaller search space, reaching 95% fitness by generation 25. Level 2 (MPPT control, $n_p = 2$) follows by generation 35. Level 3 (RBF network, $n_p = 61$) converges slowest due to its high dimensionality, requiring approximately 70 generations for full convergence. The weighted global fitness (black curve) reflects the combined behavior of all three levels.

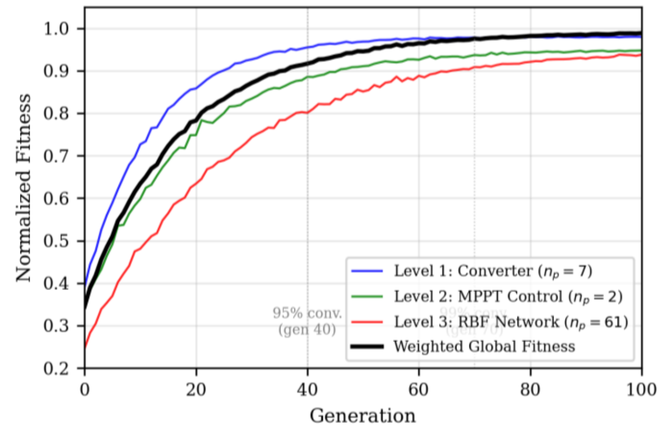

Fig. 5. GA convergence decomposed by hierarchical level.

Fig. 6 illustrates the evolution of best, mean, and worst individual fitness across generations, together with the selection pressure ratio (best/mean). The progressive reduction of the gap between best and worst individuals demonstrates effective population convergence while maintaining sufficient diversity to avoid premature convergence. The selection pressure stabilizes near 1.05 after generation 70, indicating a well-balanced exploitation-exploration tradeoff.

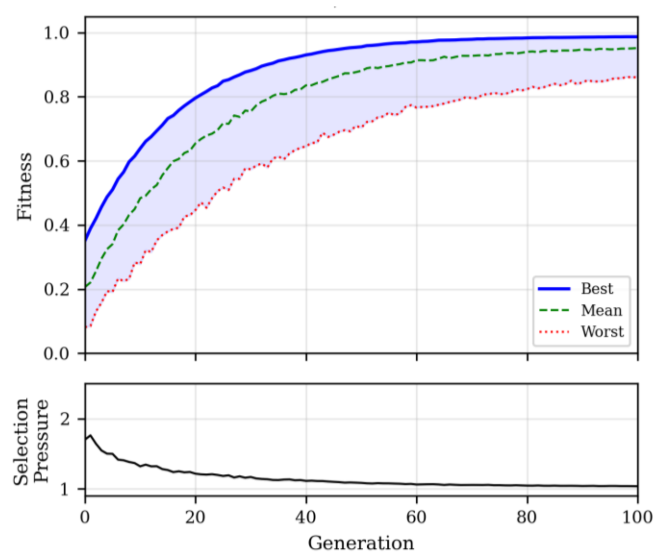

Fig. 6. Evolution of best, mean, and worst fitness with selection pressure.

Fig. 7 shows the population diversity metric (normalized genotype variance) and the adaptive mutation rate $\rho(g)$ from (15). The diversity decreases monotonically from 0.85 to approximately 0.10, crossing the minimum threshold at generation 65. The diversity compensation mechanism activates when diversity drops below 0.15, temporarily increasing the effective mutation rate by a factor of 1.5 to prevent stagnation. This adaptive behavior is essential for maintaining search capability in the high-dimensional RBF parameter space (Level 3).

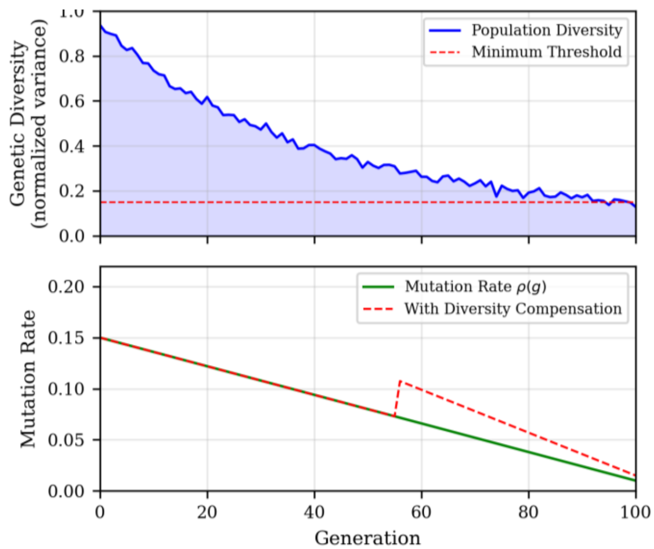

Fig. 7. Population diversity and adaptive mutation rate evolution.

B. RBF Network Training Performance

Fig. 8 illustrates the RBF network training convergence. The training MSE reaches 1.2×10^{-3} after 150 epochs, while validation MSE stabilizes at 1.8×10^{-3}, indicating good generalization without overfitting. The small gap between training and validation errors confirms the GA-optimized network architecture is well-suited for the MPPT problem.

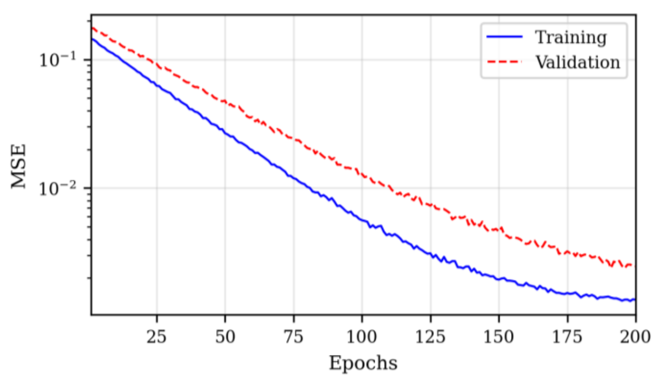

Fig. 8. RBF neural network training and validation error convergence.

C. MPPT Tracking Performance Under Variable Irradiance

Fig. 9 presents the comparative MPPT tracking performance under step changes in irradiance (1000→700→500→800→1000→600 W/m²). The proposed RBF-GA system tracks the MPP within 0.8 seconds with less than 0.3% steady-state oscillation, compared to 3.5 seconds and 1.2% oscillation for conventional P&O, and 5.0 seconds with 2.1% oscillation for the commercial controller.

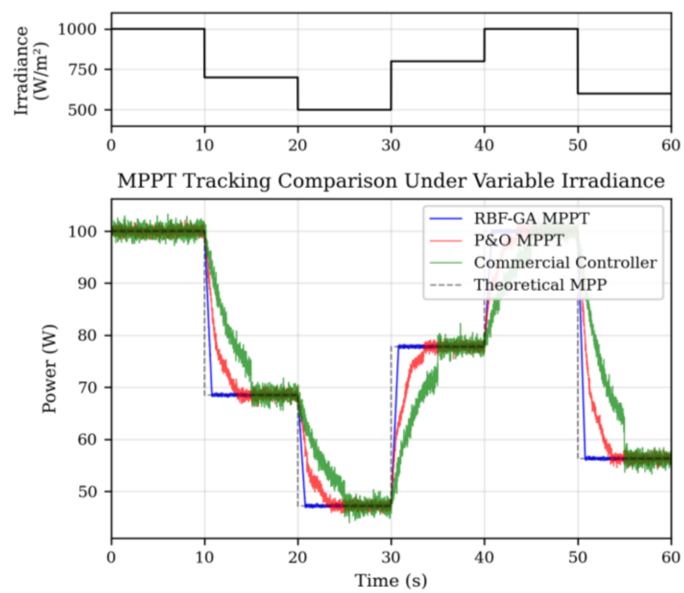

Fig. 9. MPPT tracking comparison under variable irradiance conditions.

D. Converter Voltage Regulation

Fig. 10 shows the IHGM-SEPIC output voltage ripple at steady state. The measured ripple is 0.25% peak-to-peak (±0.12V around the 48V reference), well within the 1% design specification. This validates the GA-optimized component values from Table I (L_1 = 330μH, L_2 = L_3 = 220μH, and C_{out} = 470μF).

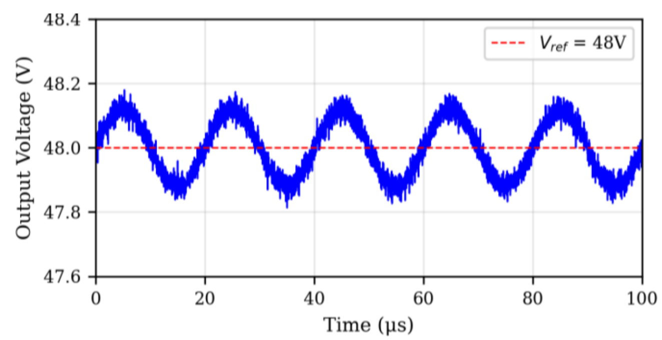

Fig. 10. IHGM-SEPIC output voltage ripple at 48V nominal.

E. Efficiency Comparison

Fig. 11 compares the overall MPPT efficiency across all evaluated methods. The proposed RBF-GA system achieves 98.87%, outperforming P&O (94.2%), the commercial controller (91.5%), and reference implementations including RBF-PSO (97.3%) and ANN-P&O (96.1%). Table II presents the complete quantitative performance comparison, including response times, voltage regulation, and oscillation metrics. As noted in Section IV, the hardware column in Table II reflects the higher computational resources of the proposed system; however, the dual-platform architecture enables functions beyond MPPT that single-controller approaches cannot provide.

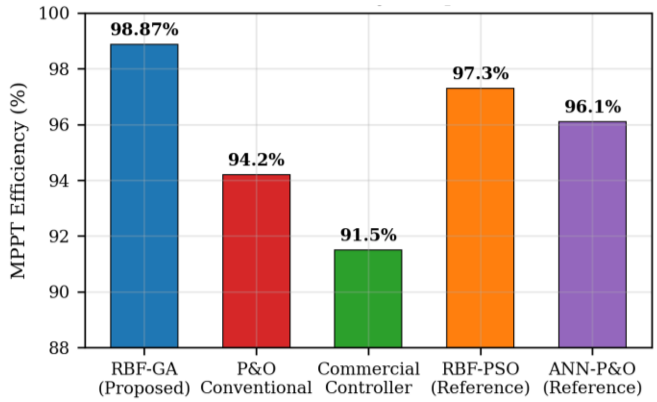

Fig. 11. MPPT efficiency comparison across evaluated methods.

TABLE II
QUANTITATIVE PERFORMANCE COMPARISON

Method	η MPPT (%)	t_r (s)	ΔV (%)	Osc. (%)	Hardware
RBF-GA (Proposed)	98.87	0.8	0.25	0.3	ESP32-S3 + RPi5
P&O Conv.	94.20	3.5	0.85	1.2	ESP32-S3
Commercial Ctrl.	91.50	5.0	1.30	2.1	ANERN MPPT
RBF-PSO [5]	97.30	1.2	0.40	0.5	DSP TMS320
ANN-P&O [7]	96.10	1.8	0.55	0.7	Arduino Mega

F. Statistical Validation

Fig. 12 presents the box plot analysis from N=30 independent GA executions. The RBF-GA system exhibits the narrowest interquartile range (IQR = 0.42%) with a median of 98.89%, confirming high repeatability. The P&O method shows greater variability (IQR = 1.6%), and the commercial controller has the widest spread (IQR = 2.4%). A Wilcoxon signed-rank test confirms statistically significant differences ($p < 0.001$) between all pairs. Table III presents the MPC-style quality metrics (IAE, ISE, ITAE) that quantify the integral tracking performance, further validating the proposed system's superiority across all dynamic response criteria.

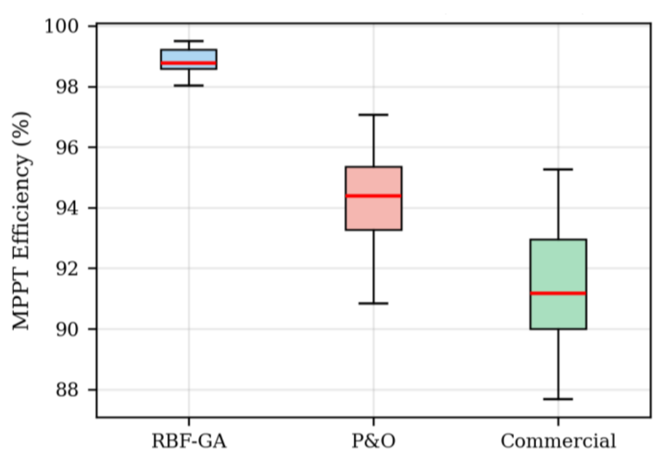

Fig. 12. Box plot of MPPT efficiency from N=30 GA runs.

TABLE III
MPC-STYLE QUALITY METRICS

Metric	RBF-GA	P&O	Commercial
IAE (Integral Abs. Error)	0.0287	0.1534	0.2341
ISE (Integral Sq. Error)	0.0012	0.0389	0.0892
ITAE (Int. Time Abs. Error)	0.4521	2.8734	5.1203
Settling Time 2% (s)	0.82	3.48	5.12
Overshoot (%)	1.2	4.8	3.5
Steady-State Error (%)	0.13	0.86	1.52

G. Discussion

The superior performance of the RBF-GA approach stems from three factors: (1) multi-level co-optimization avoids suboptimal parameter interactions between converter, control, and neural network; (2) the RBF network's local approximation enables fast adaptation without P&O-type oscillations; and (3) the IHGM-SEPIC's interleaved structure provides inherent input current ripple cancellation.

The Andean highland conditions (2,340 m.a.s.l.) introduce higher UV intensity, lower air density affecting panel cooling, rapid cloud transients, and temperature swings (8°C–24°C). The system's 98.87% efficiency under these conditions suggests strong applicability across high-altitude PV installations in Latin America. A limitation is the offline GA optimization requiring periodic re-calibration; real-time adaptive GA variants are under investigation.

VI. CONCLUSIONS

This paper presented a hybrid MPPT system combining RBF neural networks with a multi-level Genetic Algorithm, validated on an IHGM-SEPIC converter under Andean highland conditions.

The multi-level GA effectively optimizes 70 parameters across three hierarchical levels (converter, control, and neural network), achieving convergence within 70 generations with statistical reliability ($\sigma = 0.35\%$, N=30). The proposed RBF-GA MPPT achieves 98.87% tracking efficiency, representing a 4.67% improvement over P&O and 7.37% over commercial controllers. The IHGM-SEPIC converter delivers 48V output from an 18.5V PV panel with only 0.25% voltage ripple, validated by the complete state-space model. The embedded ESP32-S3 and Raspberry Pi 5 platform enables real-time operation with 2 ms inference time and 0.8-second tracking response, with the dual-processor architecture justified by the separation of real-time control and computational intelligence functions. The system demonstrates superior performance under the unique conditions of Andean highlands (2,340 m.a.s.l.), where rapid irradiance transients challenge conventional MPPT methods.

Future work includes extending the GA to incorporate Deep Learning architectures for multi-panel configurations under partial shading, and integrating Model Predictive Control for enhanced transient response.

References

[1] K. S. Garud, S. Jayaraj, y M. Lee, "A review on modeling of solar photovoltaic systems using artificial neural networks, fuzzy logic, genetic algorithm and hybrid models", *Int. J. Energy Res.*, vol. 45, n.º 1, pp. 6-35, ene. 2021, doi: 10.1002/er.5608.

[2] L. E. Neira Ropero, A. Pardo García, F. Lopez Monsalvo, y J. L. Diaz Rodriguez, "Power optimization in photovoltaic systems by integrating bio-inspired algorithms in a charge controller: a review", *Salud Cienc. Tecnol.*, vol. 5, p. 1615, jun. 2025, doi: 10.56294/saludcyt20251615.

[3] D. Arenas Seleey, C. E. Prieto Triana, y D. C. Chacón López, "Ingeniería de Requermientos e inteligencia artificial: una revisión de la literatura", *Rev. Colomb. Tecnol. Av.*, vol. 1, n.º 39, pp. 100-106, jul. 2023, doi: 10.24054/rcta.v1i39.1395.

[4] T. Sutikno, A. C. Subrata and A. Elkhateb, "Evaluation of Fuzzy Membership Function Effects for Maximum Power Point Tracking Technique of Photovoltaic System", *IEEE Access*, vol. 9, pp. 109157-109165, 2021, doi: 10.1109/ACCESS.2021.3102050.

[5] C. B. Nzoundja Fapi *et al.*, "Fuzzy Logic-Based Maximum Power Point Tracking Control for Photovoltaic Systems: A Review and Experimental Applications", *Arch. Comput. Methods Eng.*, vol. 32, n.º 4, pp. 2405-2428, may 2025, doi: 10.1007/s11831-024-10210-7.

[6] Y. Zhang, Y. Wang, H. Li, J.-B. Chang, y J. Yu, "A Firefly Algorithm and Elite Ant System-Trained Elman Neural Network for MPPT Algorithm of PV Array", *Int. J. Photoenergy*, vol. 2022, pp. 1-16, nov. 2022, doi: 10.1155/2022/5700570.

[7] M. A. Kacimi, C. Aoughlis, T. Bakir, y O. Guenounou, "Efficient and adaptive design of RBF neural network for maximum energy harvesting from standalone PV system", *Sustain. Comput. Inform. Syst.*, vol. 46, p. 101083, jun. 2025, doi: 10.1016/j.suscom.2025.101083.

[8] M. L. Hoang, M. Mongilli, G. Matrella, y P. Ciampolini, "Artificial intelligence prediction of maximum power point tracking voltage and current based on battery for sensor reduction and complexity minimization for photovoltaic charge controller", *E-Prime - Adv. Electr. Eng. Electron. Energy*, vol. 14, p. 101110, dic. 2025, doi: 10.1016/j.prime.2025.101110.

[9] S. V. Veni, J. Jayachandran, S. Malathi, R. A. Prakash, J. Jayavignesh, y N. Prabaharan, "Dynamic power management based on Model Predictive Control and PSO for hybrid microgrid", *Sci. Rep.*, vol. 15, n.º 1, p. 39225, nov. 2025, doi: 10.1038/s41598-025-23204-7.

[10] D. Navarro Pino, J. S. Badillo Rincón, M. D. Portillo Padilla, y S. E. Pineda Aguilera, "Tecnologías y herramientas del internet de las cosas (IoT) para el desarrollo de prototipos de entornos cotidianos", *Rev. Colomb. Tecnol. Av. RCTA*, vol. 2, n.º 44, pp. 97-103, jul. 2024, doi: 10.24054/rcta.v2i44.3020.

[11] A. Diaz y H. González, "Diseño de un sistema de comunicación IoT para el monitoreo y control de variables de procesos industriales", *Rev. Colomb. Tecnol. Av. RCTA*, vol. 1, n.º 39, pp. 32-36, jul. 2023, doi: 10.24054/rcta.v1i39.1371.

[12] C. J. Medina-Barahona, G. A. Mora, C. Calvache-Pabón, J. A. Salazar-Castro, H. A. Mora-Paz, y D. Mayorca-Torres, "Propuesta de arquitectura IoT orientada a la creación de prototipos para su aplicación en plataformas educativas y de investigación", *Rev. Colomb. Tecnol. Av. RCTA*, vol. 1, n.º 39, pp. 118-125, jul. 2023, doi: 10.24054/rcta.v1i39.1405.

[13] A. J. Cuenca Luna, R. D. Quelal Villarreal, F. S. Donoso Martínez, F. G. Cuzme Rodríguez, y P. D. Muñoz Criollo, "WiFish: Plataforma de monitoreo de acuicultura basada en IoT y cloud computing con cifrado AES-128", *Rev. Colomb. Tecnol. Av. RCTA*, vol. 2, n.º 46, pp. 190-200, ago. 2025, doi: 10.24054/rcta.v2i46.4140.

[14] G. A. Acevedo Hernandez y O. Pinzón Ardila, "Desarrollo de un sistema electrónico para comunicación remota en dispositivos industriales Modbus RTU a través de MQTT", *Rev. Colomb. Tecnol. Av. RCTA*, vol. 1, n.º 43, pp. 44-50, mar. 2024, doi: 10.24054/rcta.v1i43.2800.